



Structural homo- and heterosynaptic plasticity in mature and adult newborn rat hippocampal granule cells

Tassilo Jungenitz^{a,b,1,2}, Marcel Beining^{a,b,c,d,1}, Tijana Radic^a, Thomas Deller^a, Hermann Cuntz^{c,d}, Peter Jedlicka^{a,3,4}, and Stephan W. Schwarzacher^{a,4}

^aInstitute of Clinical Neuroanatomy, Goethe University Frankfurt, 60323 Frankfurt am Main, Germany; ^bFaculty of Biosciences, Goethe University Frankfurt, 60323 Frankfurt am Main, Germany; ^cErnst Strüngmann Institute for Neuroscience in Cooperation with Max Planck Society, 60528 Frankfurt am Main, Germany; and ^dFrankfurt Institute for Advanced Studies, 60438 Frankfurt am Main, Germany

Edited by Fred H. Gage, The Salk Institute for Biological Studies, San Diego, CA, and approved April 2, 2018 (received for review February 16, 2018)

Adult newborn hippocampal granule cells (abGCs) contribute to spatial learning and memory. abGCs are thought to play a specific role in pattern separation, distinct from developmentally born mature GCs (mGCs). Here we examine at which exact cell age abGCs are synaptically integrated into the adult network and which forms of synaptic plasticity are expressed in abGCs and mGCs. We used virus-mediated labeling of abGCs and mGCs to analyze changes in spine morphology as an indicator of plasticity in rats in vivo. High-frequency stimulation of the medial perforant path induced long-term potentiation in the middle molecular layer (MML) and long-term depression in the nonstimulated outer molecular layer (OML). This stimulation protocol elicited NMDA receptor-dependent homosynaptic spine enlargement in the MML and heterosynaptic spine shrinkage in the inner molecular layer and OML. Both processes were concurrently present on individual dendritic trees of abGCs and mGCs. Spine shrinkage counteracted spine enlargement and thus could play a homeostatic role, normalizing synaptic weights. Structural homosynaptic spine plasticity had a clear onset, appearing in abGCs by 28 d postinjection (dpi), followed by heterosynaptic spine plasticity at 35 dpi, and at 77 dpi was equally as present in mature abGCs as in mGCs. From 35 dpi on, about 60% of abGCs and mGCs showed significant homo- and heterosynaptic plasticity on the single-cell level. This demonstration of structural homo- and heterosynaptic plasticity in abGCs and mGCs defines the time course of the appearance of synaptic plasticity and integration for abGCs.

adult neurogenesis | hippocampus | structural plasticity | heterosynaptic plasticity | rat

Hippocampal granule cells (GCs) are generated throughout life in the mammalian dentate gyrus (DG) (1) and are considered important for spatial learning and memory (2). Adult newborn GCs (abGCs) are thought to play a distinct role in the separation and identification of new patterns, whereas mature GCs (mGCs), born during development, enable the completion of stored patterns upon partial activation (3, 4). The generation and maturation of GCs follow a course of differentiation, structural growth, and functional integration (5). Within 3–11 wk of cell age, abGCs become increasingly integrated into the hippocampal network (6, 7). This particular function of abGCs might depend on a critical time window at 3–6 wk when abGCs exhibit enhanced synaptic plasticity (8–11), an increased excitation-to-inhibition balance (12, 13), and the capability for experience-dependent remodeling of their connectivity (14).

Dendritic spines of abGCs appear during the third week (15), forming first glutamatergic contacts at perforant path synapses (16, 17). Spine size has been reported to match the size of the postsynaptic density (PSD) and the number of glutamate receptors and therefore is directly correlated with synaptic strength (18–20). Several studies demonstrated that induction of long-term potentiation (LTP) is associated with spine enlargement (21), and conversely, long-term depression (LTD) is associated with spine

shrinkage (22). Thus, change in spine size can be seen as a structural correlate of LTP and LTD. These two opposing types of synaptic plasticity (23) can be further classified into homosynaptic and heterosynaptic plasticity. Homosynaptic plasticity is induced at synapses that are directly stimulated, while heterosynaptic plasticity takes place at inactive synapses neighboring the stimulated synapses (23).

Excitatory synaptic contacts impinge on GC dendrites in the molecular layer (ML) of the DG. The ML is highly laminated and receives inputs via the medial perforant path (MPP) in the middle molecular layer (MML) and via the lateral perforant path (LPP) in the outer molecular layer (OML) as well as inputs from associated and commissural fibers of mossy cells in the inner molecular layer (IML) (24).

In previous studies, selective stimulation of either the MPP or LPP induced homosynaptic LTP (25) and heterosynaptic LTD (26) in the respective MML or OML. Heterosynaptic LTD has been recently discussed as a homeostatic mechanism for normalizing the overall synaptic weights and maintaining synaptic competition (27). Furthermore, computational modeling showed

Significance

The lifelong genesis of hippocampal granule cells (abGCs) enables specific forms of spatial learning. We analyzed which forms of synaptic plasticity are present in abGCs in comparison with mature granule cells (mGCs). We found structural equivalents of homosynaptic long-term potentiation and heterosynaptic long-term depression, two fundamental forms of cellular learning. abGCs and mGCs showed spine enlargement on stimulated segments and spine shrinkage on nonstimulated segments concurrently present on dendrites of individual cells, indicating a sharpening and a homeostatic regulation of synaptic efficacy. abGCs expressed homo- and heterosynaptic spine plasticity with a clear onset between 4–5 wk of cell age, demonstrating increasing synaptic plasticity during the phase of abGC integration on the structural level.

Author contributions: T.J., M.B., T.R., T.D., H.C., P.J., and S.W.S. designed research; T.J. and M.B. performed research; T.J. and M.B. analyzed data; and T.J., M.B., T.D., P.J., and S.W.S. wrote the paper.

The authors declare no conflict of interest.

This article is a PNAS Direct Submission.

Published under the PNAS license.

¹T.J. and M.B. contributed equally to this work.

²To whom correspondence should be addressed. Email: tassilo.j@gmx.de.

³Present addresses: ICAR3R – Interdisciplinary Centre for 3Rs in Animal Research, Justus Liebig University Giessen, 35390 Giessen, Germany; and Frankfurt Institute for Advanced Studies, 60438 Frankfurt am Main, Germany.

⁴P.J. and S.W.S. contributed equally to this work.

This article contains supporting information online at www.pnas.org/lookup/suppl/doi:10.1073/pnas.1801889115/-DCSupplemental.

Published online April 30, 2018.

that homosynaptically induced LTP would strengthen heterosynaptic LTD at neighboring dendritic segments (28) and thus could lead to effective and long-lasting changes in synaptic weights as a requisite for learning and memory. How and when heterosynaptic plasticity emerges during development and contributes to the integration of abGCs into the hippocampal network is currently not known.

We performed intrahippocampal injections of viral vectors for GFP labeling of abGCs and mGCs to study the time course of the development and structural plasticity of their dendritic spines. In vivo high-frequency stimulation (HFS) of the MPP induced enlargement of spines located in the MML in abGCs from 21 d post injection (dpi) on. Furthermore, neighboring spines in the unstimulated IML and OML of the same dendritic tree exhibited shrinkage. Thus, we could demonstrate the occurrence of homo- and heterosynaptic structural plasticity in abGCs.

Results

HFS of the Perforant Path Induced Expression of Arc in DG abGCs and mGCs. The population of abGCs was transduced with a GFP-expressing murine leukemia retroviral vector (RV-GFP) in 8- to 13-wk-old male Sprague–Dawley rats by an intrahippocampal injection followed by HFS of the MPP at distinct time points between 21 and 77 dpi, to analyze the time course of development and structural plasticity of spines under in vivo conditions (Fig. 1 *A* and *J–M*). Furthermore, we used intrahippocampal injections of an adeno-associated viral (AAV) vector to express GFP under the control of a synapsin promoter to study developmentally born mGCs (Fig. 1 *A*, *N*, and *O*). We refer to RV-GFP- and AAV-GFP-labeled cells as “abGCs” and “mGCs,” respectively in the remaining text, although it is worth noting that AAV-GFP labeling does not exclude mature adult-born GCs (*Methods*). We then performed 2-h HFS of the MPP with a protocol that induced robust LTP as well as a strong expression of immediate early genes (IEGs) in more than 90% of all GCs (Fig. 1 *B* and *F* and refs. 23 and 27). In addition, 2-h HFS resulted in enhanced expression of the LTP marker F-actin (29) in the ipsilateral MML, i.e., the lamina of MPP fiber projection (see Fig. 3). Following 2-h HFS, expression of the synaptic plasticity-related IEG Arc was detected in the great majority of GCs in the ipsilateral DG, including abGCs and mGCs (Fig. 1 *K*, *M*, and *O*). LTP induction at the MPP is known to generate a concurrent heterosynaptic LTD of the LPP input (26, 30). To evaluate the occurrence of heterosynaptic LTD following HFS of the MPP, we placed a second stimulation electrode in the LPP in control experiments. Stimulation of the LPP was discriminated from the concurrent MPP stimulation by characteristic differences in the shape of the evoked local GC field potentials and in the latency of the population spike (Fig. 1 *C* and ref. 24 and 29). Furthermore, low-intensity paired-pulse stimulation typically evoked paired-pulse facilitation at a 20-ms interpulse interval following LPP, whereas MPP stimulation evoked paired-pulse depression, as described earlier (Fig. 1 *D* and *E* and ref. 31). Following 2-h HFS, homosynaptic LTP at the MPP was accompanied by heterosynaptic LTD at the LPP (Fig. 1 *F* and *G*). The contralateral, nonstimulated DG showed no LTP induction following HFS in control recordings and no enhancement of Arc expression in the granule cell layer (GCL) as well as no enhancement of F-actin in all stimulation experiments (Fig. 1 *H–J*, *L*, and *N*). The contralateral DG therefore served as a control and was used to study the general time course of spine development in abGCs.

Time Course of Spine Development in abGCs. Dendritic segments of abGCs (Fig. 2*A*, *Upper*) and mGCs (Fig. 2*A*, *Lower*) were sampled from the IML, MML, and OML of the contralateral, unstimulated DG (Fig. 2*C*). Only segments with a direct traceable connection to the soma were used. Time points for the analysis of abGC spines were chosen based on previous findings from rats in vivo (32),

starting at 21 dpi ($n = 3$ animals), with additional time points at 28 ($n = 6$), 35 ($n = 5$), and 77 ($n = 4$) dpi, and were compared with mGCs ($n = 6$). Dendritic segments in GCs showed a high diversity of spine sizes and shapes. Spines were classified into small ($<0.2 \mu\text{m}^2$) and large ($>0.2 \mu\text{m}^2$) spines using a grid-based approach (Fig. 2*B*; for details see *Methods*). The density of spines, irrespective of size, increased gradually in all layers (IML, MML, and OML) between 21 and 77 dpi: starting at 21 dpi with $0.84 \pm 0.02 \mu\text{m}^{-1}$ in the IML, $0.99 \pm 0.01 \mu\text{m}^{-1}$ in the MML, and $0.95 \pm 0.18 \mu\text{m}^{-1}$ in the OML and reaching mature levels with $1.41 \pm 0.09 \mu\text{m}^{-1}$ in the IML, $1.58 \pm 0.04 \mu\text{m}^{-1}$ in the MML, and $1.77 \pm 0.13 \mu\text{m}^{-1}$ in the OML at 77 dpi (Fig. 2*D*₁). At 77 dpi, the spine density of abGCs showed no significant differences from mGCs in all layers (IML: $1.30 \pm 0.12 \mu\text{m}^{-1}$, MML: $1.42 \pm 0.11 \mu\text{m}^{-1}$, OML: $1.48 \pm 0.09 \mu\text{m}^{-1}$). Both small (Fig. 2*E*₁) and large (Fig. 2*F*₁) spines exhibited a similar gradual, age-dependent increase in density throughout all MLs, reaching the density of mGCs at 77 dpi. The density of small spines in abGCs increased from $0.82 \pm 0.04 \mu\text{m}^{-1}$ at 21 dpi to $1.35 \pm 0.07 \mu\text{m}^{-1}$ at 77 dpi, not significantly different from the density of mGCs ($1.18 \pm 0.10 \mu\text{m}^{-1}$). The density of large spines in mGCs increased from $0.10 \pm 0.02 \mu\text{m}^{-1}$ at 21 dpi to $0.22 \pm 0.03 \mu\text{m}^{-1}$ at 77 dpi with large spine density in mGCs being $0.18 \pm 0.02 \mu\text{m}^{-1}$. Thus, large spines formed about 15% of the spine density, and there was no significant change in the percentage of large spines over the entire time period that we analyzed (Fig. 2*G*₁). Data from all analyzed animals were pooled to perform a layer-specific, cell age-independent comparison. Spine density (including small and large spines) in the MML and OML was significantly higher than in the IML (Fig. 2 *D*_{2–*F*2}). However, the MML showed a higher percentage of large spines than the IML (Fig. 2*G*₂).

We conclude from these results that a gradual development of spines occurs in abGCs between 21 and 77 dpi, when spine size and density reach the levels found in mGCs.

HFS of the Perforant Path Induced a Layer-Specific Expression of F-Actin.

F-actin is located in dendritic spines and is involved in processes regulating structural modifications of spines related to synaptic plasticity (29, 33). F-actin expression has been described as a valuable tool to measure layer-specific synaptic activation and plasticity following LTP induction in vivo (29). Following 2-h HFS of the MPP, F-actin expression was increased in the MML, i.e., the lamina of MPP fiber projection (Fig. 3*A* and *B*). The distribution of F-actin fluorescence intensity in the IML, MML, and OML was measured along the GCL–hippocampal fissure axis, starting from the border between the GCL and IML up to the hippocampal fissure (Fig. 3*C*). Following HFS, F-actin fluorescence intensity showed a significant elevation in the stimulated MML and a significant reduction in the unstimulated IML and OML, whereas the fluorescence intensity of the total ML was not altered compared with the unstimulated side (Fig. 3*D*). There was no detectable difference in the F-actin distribution throughout the ML in the contralateral hemisphere of stimulated animals and naive control animals without any stimulation (Fig. 3*C*).

Taken together, these results show stimulation-dependent and layer-specific accumulation of F-actin within the MML and a concurrent decrease of signal intensity in the adjacent IML and OML following HFS of the MPP. These data indicate a stimulation-induced homosynaptic LTP in the MML (29) and a concurrent depression in the IML and OML, which could correspond to heterosynaptic LTD in the OML (26), and a possible similar effect in the IML.

Structural Plasticity of Dendritic Spines in abGCs Following 2-h Perforant Path HFS.

We then took advantage of known correlations between spine size and synaptic strength (20) to study the effects of HFS on structural spine plasticity. We again used the grid-based spine size classification (Fig. 2*B*) to discriminate between

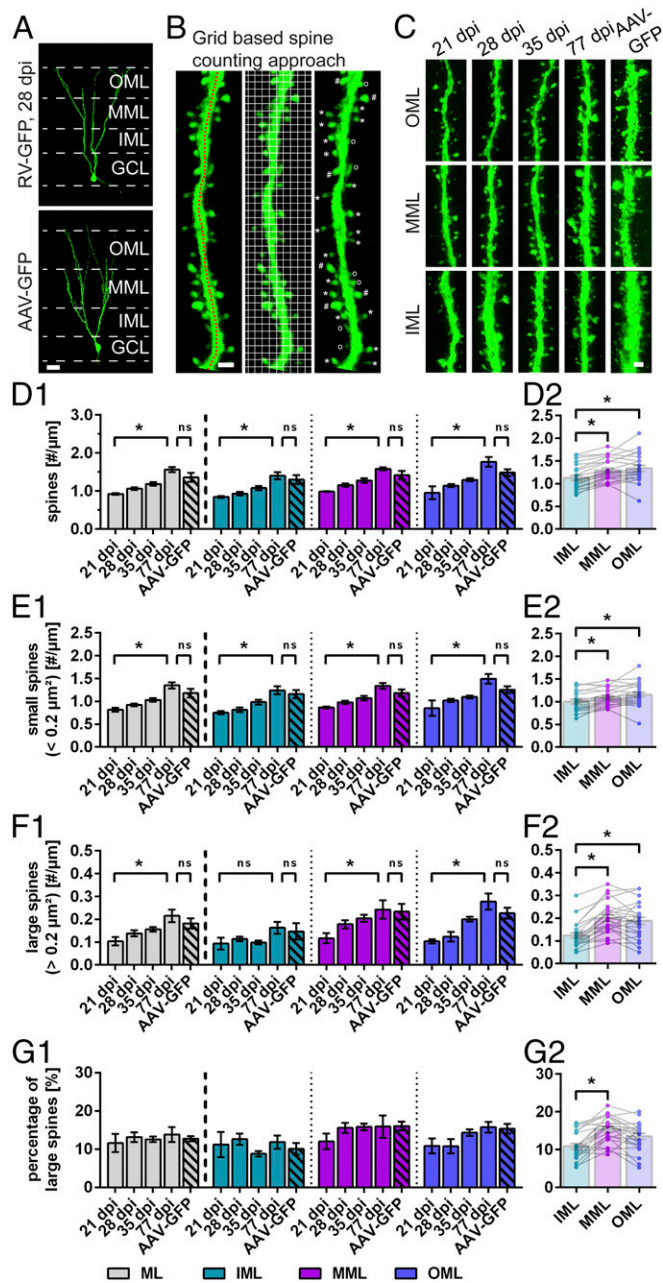


Fig. 2. Time course of dendritic spine development in abGCs. (A) Sample RV-GFP-labeled abGC at 28 dpi and AAV-GFP-labeled mGC used to quantify dendritic spines in the IML, MML, and OML during the development of abGCs and in mGCs. (B) The length of a dendritic segment was measured in a z-projection (Left, red dotted line), and a grid-based approach (Center, grid size $0.2 \mu\text{m}^2$) was used to determine the density of spines in general and to differentiate between small ($<0.2 \mu\text{m}^2$, indicated by stars) and large ($>0.2 \mu\text{m}^2$, indicated by dashes) spines (Right). Spines without a spine neck and head (indicated by open circles) were excluded from analysis. (C) Samples of dendritic segments from 21 to 77 dpi abGCs and mGCs showing spines in the IML, MML, and OML. (D1) Density of spines in RV-GFP-labeled abGCs in the complete ML from 21 to 77 dpi and in AAV-GFP-labeled mGCs. (D2) Density of spines per layer (pooled data from all animals). (E1) Density of small spines. (E2) Density of small spines per layer (pooled data from all animals). (F1) Density of large spines in the IML, MML, and OML. (F2) Density of large spines per layer (pooled data from all animals). (G1) Percentage of large spines was calculated as the relative amount of large spines from spine density. (G2) Overall percentage of large spines per layer (pooled data from all animals). Number of animals: $n_{21 \text{ dpi}} = 3$; $n_{28 \text{ dpi}} = 6$; $n_{35 \text{ dpi}} = 5$; $n_{77 \text{ dpi}} = 4$; $n_{\text{AAV-GFP}} = 6$. D1-G1: $*P < 0.05$, Kruskal-Wallis with Dunn's multiple comparisons test, 21 dpi vs. 77 dpi and 77 dpi vs. mGCs. D2-G2: $*P < 0.05$, Friedman with Dunn's multiple comparisons test, IML vs. MML, IML vs. OML, and MML vs. OML. (Scale bars: $25 \mu\text{m}$ in A; $1 \mu\text{m}$ in B and C.) H, hilus.

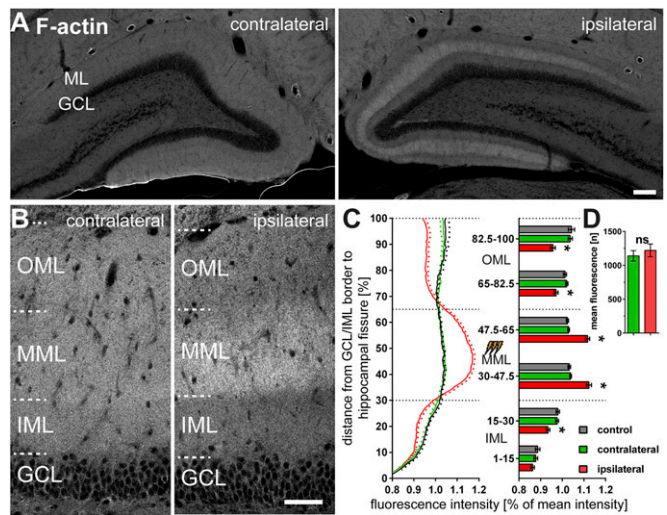


Fig. 3. F-actin is enhanced in the MML following 2-h HFS of the MPP. (A and B) Expression of F-actin following 2-h HFS. (C) Normalized intensity profiles obtained across the ML (from the GCL-IML border to the hippocampal fissure) revealed layer-specific changes of F-actin expression on the stimulated ipsilateral side (red trace and bars) compared with the contralateral side (green line and bars) and with control animals (gray line and bars). (D) Immunofluorescence intensity of the entire ML was not altered following HFS in the stimulated ipsilateral side (red bar) versus the unstimulated contralateral side (green bar). Number of animals: $n_{\text{contralateral}} = 21$; $n_{\text{ipsilateral}} = 21$; $n_{\text{control}} = 8$. C: $*P < 0.05$, two-way ANOVA with Bonferroni correction. D: $*P < 0.05$, two-sided Wilcoxon rank-sum test. (Scale bars: $100 \mu\text{m}$ in A; $50 \mu\text{m}$ in B.) contra, contralateral; H, hilus; ipsi, ipsilateral.

small ($<0.2 \mu\text{m}^2$) and large ($>0.2 \mu\text{m}^2$) spines and again analyzed only those dendritic compartments that could be traced to the cell soma. Within the MML, following 2-h HFS, the spine density remained unchanged at any age in both abGCs and mGCs (Fig. 4C). However, we observed a decrease in the density of small spines (Fig. S1C) and an increase in density of large spines (Fig. S1D) in stimulated abGCs. The result was a significant gain in the percentage of large spines within the ipsilateral MML of abGCs (Fig. 4D) at 28 dpi (from $15.55 \pm 1.32\%$ to $24.50 \pm 1.35\%$), at 35 dpi (from $15.83 \pm 0.89\%$ to $22.39 \pm 2.35\%$), and at 77 dpi (from $15.90 \pm 2.93\%$ to $26.48 \pm 1.70\%$), as well as in mGCs (from $16.06 \pm 1.12\%$ to $28.56 \pm 3.02\%$). Thus, HFS of the MPP induced structural plasticity and spine enlargement in the MML in abGCs from 28 dpi on, as well as in mGCs.

While the total number of spines of abGCs and mGCs also remained unchanged in the adjacent OML (Fig. 4A), there was a trend toward increased density of small spines (Fig. S1A), and the density of large spines decreased (Fig. S1B), together resulting in a significant decline in the percentage of large spines in the OML from 35 dpi on (from $14.31 \pm 0.82\%$ to $8.22 \pm 0.33\%$ at 35 dpi and from $15.73 \pm 1.39\%$ to $8.80 \pm 1.28\%$ at 77 dpi) and in mGCs (from $15.33 \pm 1.30\%$ to $9.38 \pm 1.65\%$) (Fig. 4B). Although a similar trend of a decline in large spines was observed in the IML, we found no significant changes in the percentage of large versus small spine sizes in the IML of abGCs and mGCs (Fig. 4E and F and Fig. S1E and F).

These results indicate that HFS of the MPP leads to robust homosynaptic spine enlargement in abGCs in the directly activated MML from 28 dpi on and in mGCs. Furthermore, concurrent heterosynaptic spine shrinkage was found in the adjacent OML in abGCs starting at 35 dpi and in mGCs. Interestingly, stimulation-induced spine enlargement in the MML and spine shrinkage in the OML were found on adjacent dendritic segments of the same identified GCs, providing structural evidence for

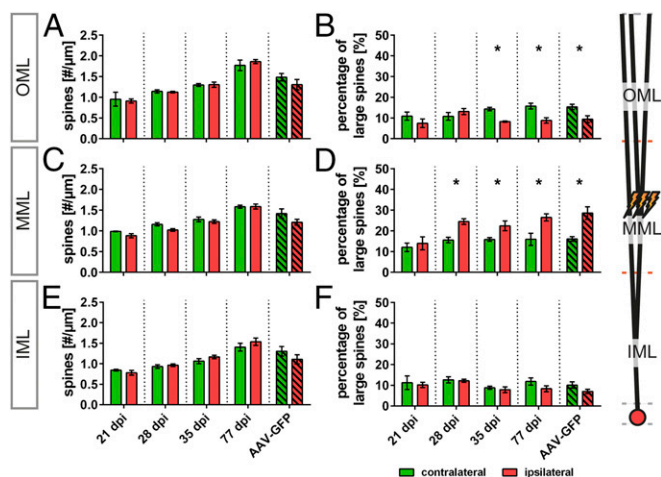


Fig. 4. The percentage of large spines is increased in the MML and decreased in the OML following 2-h HFS of the MPP. The MPP was stimulated with a strong HFS protocol for 2 h to induce LTP in the ipsilateral MML. Dendritic spines of RV-GFP-labeled abGCs (21–77 dpi) or AAV-GFP-labeled mGCs were analyzed in a layer-specific manner. The contralateral, nonstimulated hemisphere was used as a control. (A) Spine density in the OML was not altered following HFS. (B) The percentage of large spines showed a significant decrease in abGCs from 28 dpi on and in mGCs. (C) Spine density in the MML did not change following stimulation at any age in abGCs or in mGCs. (D) The percentage of large spines increased significantly in abGCs from 28 dpi on and in mGCs. (E and F) In this analysis, spines in the IML were not significantly affected by HFS (but see Fig. 5B). Number of animals: $n_{21 \text{ dpi}} = 3$; $n_{28 \text{ dpi}} = 6$; $n_{35 \text{ dpi}} = 5$; $n_{77 \text{ dpi}} = 4$; $n_{\text{AAV-GFP}} = 6$. * $P < 0.05$, two-sided Wilcoxon rank-sum test.

activity-dependent localized spine plasticity in the same neuron under in vivo conditions.

We found a sharp increase in structural spine plasticity between 28 and 35 dpi indicating a critical time window for synaptic integration of abGCs. To elucidate the gradual changes of spine size following HFS in more detail, we performed a direct measurement of the largest cross-sectional area of all spine heads in confocal z-stacks of dendritic segments from RV-GFP-labeled abGCs at 28 and 35 dpi (Fig. 5).

The average area of spine heads in the MML increased from $0.13 \pm 0.01 \mu\text{m}^2$ at 28 dpi to $0.160 \pm 0.002 \mu\text{m}^2$ at 35 dpi in abGCs contralateral to the stimulation. We applied thresholds of $0.15 \mu\text{m}^2$, $0.2 \mu\text{m}^2$, and $0.25 \mu\text{m}^2$ to these datasets to differentiate between small and large spines and to analyze the size changes of larger spines (Fig. 5A–F, *Insets*). At 28 dpi, spines in the MML were affected by 2-h HFS (Fig. 5C) as indicated by an increase from $14.09 \pm 1.65\%$ to $22.01 \pm 1.66\%$ (threshold of $0.2 \mu\text{m}^2$). There were no significant changes in the OML (Fig. 5A) and the IML (Fig. 5E) following HFS. At 35 dpi, abGCs in the MML at a threshold of $0.25 \mu\text{m}^2$ showed an increase in spine head size from $12.45 \pm 0.51\%$ to $18.24 \pm 3.62\%$ (Fig. 5D). In contrast, at a threshold of $0.2 \mu\text{m}^2$, spines in the OML and IML (Fig. 5B and F) showed a decrease in size (OML: from $20.19 \pm 2.90\%$ to $10.51 \pm 0.70\%$; IML: from $11.66 \pm 1.08\%$ to $5.02 \pm 0.72\%$). The existence of synaptic contacts on labeled abGCs spines within the MML was verified with ultrastructural examination of abGCs at 35 dpi (Fig. 5G and H).

In summary, the detailed measurements of spine head size (Fig. 5) confirmed the grid-based size classification with a chosen threshold of $0.2 \mu\text{m}^2$ (Fig. 4) and showed once more the suitability of this method to detect homosynaptic structural plasticity in the MML and heterosynaptic plasticity in the OML. Furthermore, the detailed analysis provided significant evidence for additional heterosynaptically induced shrinkage of spines in the IML following HFS in abGCs at 35 dpi.

Homo- and Heterosynaptic Structural Plasticity Is Blocked by the NMDA Receptor Antagonist MK-801. To provide evidence that the structural changes in spine size are causally linked to the induction of LTP and LTD, we decided to block LTP and concurrent LTD by application of Dizocilpine maleate (MK-801). MK-801 is an uncompetitive antagonist of the NMDA receptor, which is known to block hippocampal LTP induction in vivo (29, 34). MK-801 was injected i.p. (2 mg/kg body weight) 150 min before HFS and repeatedly at 30-min intervals (0.5 mg/kg body weight) starting 30 min before HFS to maintain a working concentration during the HFS (Fig. 6A). Both LTP induction at the MPP and concurrent induction of heterosynaptic LTD at the LPP following HFS were completely blocked under the effect of MK-801 (Fig. 6B–E). LTP-dependent up-regulation of Arc in the GCL and F-actin in the MML was also fully repressed by MK-801 (Fig. 6F and G). Furthermore, a detailed layer-specific

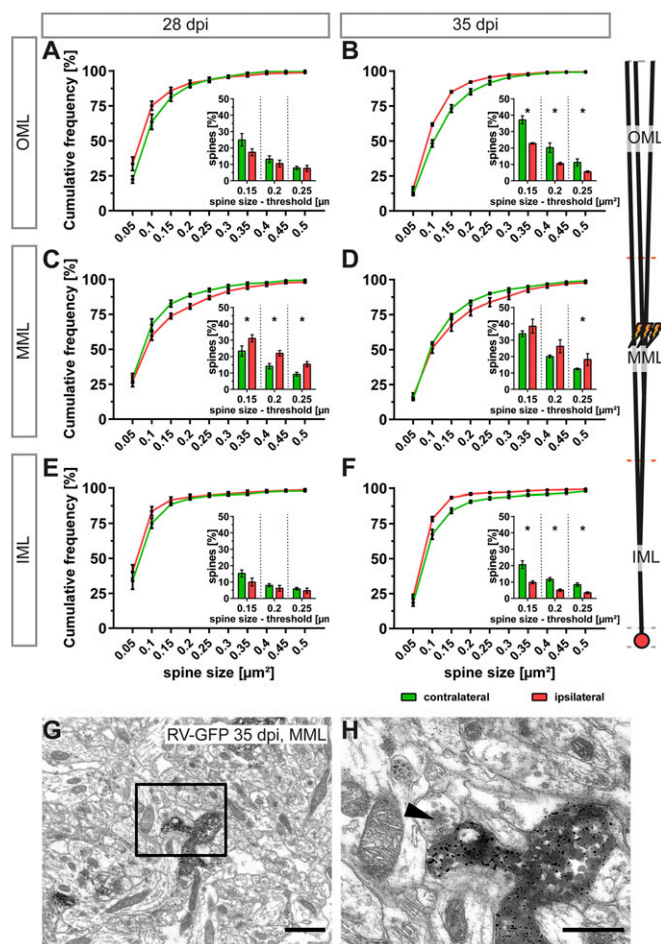


Fig. 5. Layer-specific spine size histograms confirm HFS-induced spine plasticity in 28-dpi and 35-dpi abGCs. (A–F) Cumulative fractions of spine head sizes (largest cross-sectional areas) with HFS (red, ipsilateral) and without HFS (green, contralateral) in OML (A and B), MML (C and D), and IML (E and F). *Insets* identify the number of spines larger than the following thresholds: $0.15 \mu\text{m}^2$, $0.2 \mu\text{m}^2$, and $0.25 \mu\text{m}^2$. Significant homosynaptic structural plasticity is seen in the MML of 28-dpi (C) and 35-dpi (D) abGCs, and significant heterosynaptic plasticity is seen in the IML (F) and OML (B) of 35-dpi abGCs. (G) Electron micrograph illustrating an immuno-labeled cross-section of a dendritic segment located in the MML with a spine of an RV-GFP-labeled abGC (35 dpi). (H) Enlarged view of the boxed area in G. The spine forms a synapse with an unlabeled axon terminal (black arrowhead). Number of animals: $n_{28 \text{ dpi}} = 6$; $n_{35 \text{ dpi}} = 5$. * $P < 0.05$, two-sided Wilcoxon rank-sum test. (Scale bars: 1,000 nm in G; 500 nm in H.)

analysis of the F-actin distribution within the ML revealed no changes, i.e., a complete repression of the LTP-dependent F-actin increase in the ipsilateral MML (Fig. 6 G–I).

As described above, the overall spine density of AAV-GFP-labeled mGCs remained unchanged following HFS (Fig. 4 A, C, and E), but the percentage of large spines showed a significant homosynaptic increase in the ipsilateral MML (Fig. 4D) and a heterosynaptic decrease in the OML (Fig. 4B), indicative of structural heterosynaptic plasticity. Following MK-801 treatment overall spine densities again remained unchanged following HFS (contralateral IML: $1.26 \pm 0.09 \mu\text{m}^{-1}$ vs. ipsilateral IML: $1.20 \pm 0.10 \mu\text{m}^{-1}$; contralateral MML: $1.39 \pm 0.07 \mu\text{m}^{-1}$ vs. ipsilateral MML: $1.32 \pm 0.08 \mu\text{m}^{-1}$; contralateral OML: $1.21 \pm 0.08 \mu\text{m}^{-1}$ vs. ipsilateral OML: $1.22 \pm 0.09 \mu\text{m}^{-1}$) (Fig. 6J). Importantly, HFS-induced structural changes in spine size in the ipsilateral MML and OML were completely blocked following application of MK-801 (percentage of large spines: $17.56 \pm 1.97\%$ in the contralateral MML vs. $15.09 \pm 0.92\%$ in the ipsilateral MML and $17.62 \pm 1.96\%$ in the contralateral OML vs. $15.11 \pm 1.84\%$ in the ipsilateral OML) (Fig. 6K).

Taken together, these results demonstrate that HFS induced homosynaptic LTP at the MPP and heterosynaptic LTD at the LPP as well as associated changes in the expression of the synaptic plasticity-related markers Arc and F-actin and that layer-specific homo- and heterosynaptic structural changes in spine sizes are NMDA receptor dependent.

Cell-Specific Homeostatic Effect of Homo- and Heterosynaptic Changes in Spine Size. To investigate the cell-specific manifestation of homo- and heterosynaptic plasticity-related changes in spines, we analyzed individual cells labeled ipsilaterally following HFS (i.e., fully activated cells) (Fig. 7 A and B). We compared them with GCs within their respective cell age group (abGCs or mGCs) on the contralateral, nonstimulated side. Only cells in which labeled dendritic segments from all three molecular layers (IML, MML, and OML) were present within the section were used. Ipsilateral labeled cells that exhibited an elevated percentage of large spines in the MML and a decrease of large spines in the IML and OML in comparison with the contralateral side were identified as homo- and heterosynaptic plasticity-positive cells (“hom-het positive”)

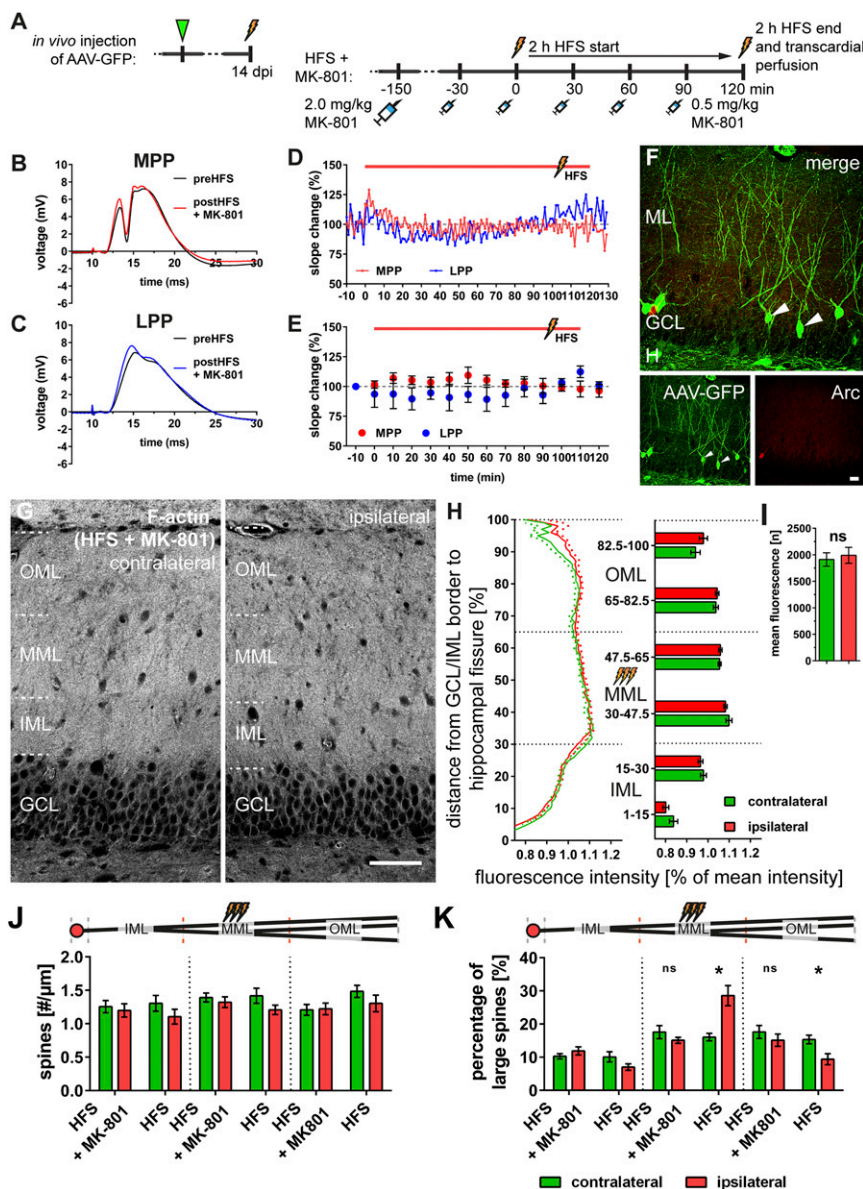
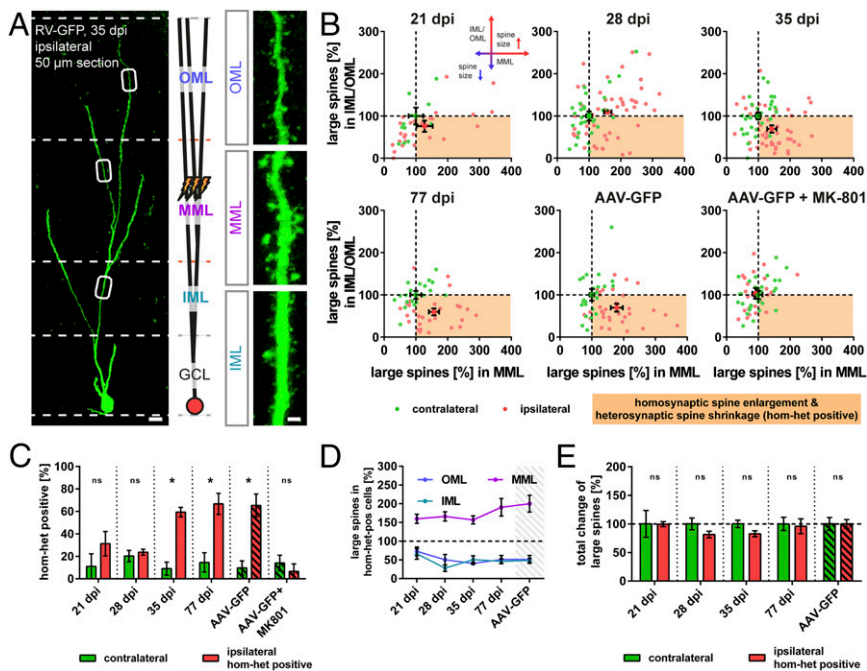


Fig. 6. Homo- and heterosynaptic structural plasticity following 2-h HFS is NMDA receptor dependent and is blocked by the application of MK-801. (A) Local bilateral intrahippocampal injections of an adeno-associated virus (AAV-GFP, synapsin promoter) were performed for GFP labeling of mature neurons. The noncompetitive NMDA receptor antagonist MK-801 was injected before and during HFS of the MPP. (B and C) Local field potentials of GCs evoked by stimulation of the MPP and the LPP were recorded in the DG. (D and E) Induction of homosynaptic LTP at the MPP and heterosynaptic LTD at the LPP following 2-h HFS was blocked by MK-801 (D, single-animal time course; E, group time course). (F) Expression of Arc (red) was not increased in the ipsilateral GCL following HFS and simultaneous application of MK-801. White arrowheads indicate AAV-GFP-labeled mGCs (green). (G) Expression of F-actin following 2-h HFS and application of MK-801. (H) Acquired intensity profiles of the ML obtained from the GCL–IML border to the hippocampal fissure revealed no layer-specific changes of F-actin expression on the stimulated ipsilateral side (red line and bars) compared with the contralateral side (green line and bars). (I) F-actin expression showed no difference between the stimulated ipsilateral hemisphere (red bar) and the unstimulated contralateral hemisphere (green bar) following HFS and simultaneous MK-801 application. (J) Dendritic spines of AAV-GFP-labeled mGCs were analyzed in a layer-specific manner. The total number of spines was not altered in any layer following HFS alone or with simultaneous MK-801 treatment. (K) Spines were categorized as small or large spines by a grid-based approach. While the percentage of large spines was increased in the MML and decreased in the OML following HFS, no structural changes in spines were observed with MK-801 treatment. Number of animals: E, $n_{\text{MPP}} = 7$ and $n_{\text{LPP}} = 4$; H and I, $n = 8$; J and K, $n_{\text{contralateral}} = 6$ and $n_{\text{ipsilateral}} = 5$. H: $*P < 0.05$, two-way ANOVA with Bonferroni correction. I: $*P < 0.05$, two-sided Wilcoxon rank-sum test. J and K: $*P < 0.05$, two-way ANOVA with Bonferroni correction, HFS+MK-801 contralateral vs. HFS+MK-801 ipsilateral and HFS contralateral vs. HFS ipsilateral. (Scale bars: 25 μm in F; 50 μm in G.) H, hilus.

Fig. 7. Homo- and concurrent heterosynaptic structural plasticity is induced within the same dendritic tree of individual GCs following 2-h HFS and can be blocked with MK-801. (A) Homo- and heterosynaptic structural remodeling of spines was analyzed in dendritic segments of the same GFP-labeled GC. (B) The entire population of analyzed GCs (28–77 dpi, AAV-GFP) at a given cell age were plotted by their changes in spine size in the IML and OML, i.e., heterosynaptic plasticity (*y* axis) versus the MML, i.e., homosynaptic plasticity (*x* axis). GCs exhibiting homosynaptic spine enlargement in the MML and heterosynaptic spine shrinkage in the IML and OML following HFS were identified as hom-het positive (orange quadrants). (C) Fraction of hom-het-positive GCs. Note that the fraction of hom-het-positive GCs increases with cell age but is strongly reduced following MK-801 treatment. (D) The increase in large spines in hom-het-positive GCs in the MML and the decrease in large spines in the IML and OML is similar in all age groups. (E) The overall percentage of large spines along the entire dendritic tree (comprising the IML, MML, and OML) relative to the contralateral side is unchanged in all age groups, indicating that structural heterosynaptic spine shrinkage in the IML and OML homeostatically counteracts the induction of homosynaptic spine enlargement in the MML. Number of animals: B–E:

$n_{21 \text{ dpi}} = 3$; $n_{28 \text{ dpi}} = 6$; $n_{35 \text{ dpi}} = 5$; $n_{77 \text{ dpi}} = 4$; $n_{\text{AAV-GFP}} = 6$; $n_{\text{AAV-GFP} + \text{MK801}} = 6$. Number of cells: $n_{21 \text{ dpi, contra}} = 12$, $n_{21 \text{ dpi, ipsi}} = 28$, $n_{28 \text{ dpi, contra}} = 34$, $n_{28 \text{ dpi, ipsi}} = 51$; $n_{35 \text{ dpi, contra}} = 30$; $n_{35 \text{ dpi, ipsi}} = 52$; $n_{77 \text{ dpi, contra}} = 19$; $n_{77 \text{ dpi, ipsi}} = 29$; $n_{\text{AAV-GFP, contra}} = 23$; $n_{\text{AAV-GFP, ipsi}} = 32$; $n_{\text{AAV-GFP} + \text{MK801, contra}} = 29$; $n_{\text{AAV-GFP} + \text{MK801, ipsi}} = 25$. C and E: * $P < 0.05$, two-sided Wilcoxon rank-sum test. D: * $P < 0.05$, 21 dpi vs. 77 dpi and 77 dpi vs. AAV-GFP, Kruskal–Wallis with Dunn’s multiple comparisons test. (Scale bars: 10 μm in A; 1 μm in B.)



cells. There was a significant increase in the percentage of hom-het positive cells at 35 dpi (ipsilateral $59.36 \pm 4.19\%$ vs. contralateral $9.05 \pm 5.85\%$), 77 dpi (ipsilateral $66.67 \pm 9.43\%$ vs. contralateral $14.58 \pm 8.59\%$), and mGCs (ipsilateral $65.28 \pm 10.17\%$ vs. contralateral $9.72 \pm 6.24\%$) following 2-h HFS (Fig. 7C). Importantly, the cell-specific structural plasticity was completely abolished in mGCs after the MK801-mediated blockage of NMDA receptors (Fig. 7C). The relative change in the percentage of large spines across all groups showed an average increase of $174.70 \pm 8.72\%$ in the MML and decreases to $47.92 \pm 6.07\%$ in the IML and to $53.21 \pm 5.31\%$ in the OML. There were no significant differences between abGCs of different cell ages or between abGCs and mGCs (Fig. 7D).

Percentages of large spines from the IML, MML, and OML of the same dendritic tree were averaged to estimate the total structural spine changes of individual abGCs (Fig. 7A and B). Interestingly, age-matched comparisons between ipsilateral and contralateral GCs revealed no significant relative differences, indicating that the overall percentage of large spines remained stable (Fig. 7E; see also Fig. 4B, D, and F). Thus, the elevation in the percentage of large spines in the ipsilateral MML by homosynaptic structural plasticity was counteracted by heterosynaptic structural plasticity in the adjacent IML and OML, which normalized the degree of structural changes along the dendritic tree.

These findings demonstrate that homo- and heterosynaptic structural plasticity is present in individual mGCs and abGCs from 35 dpi on.

Discussion

In this study we show homosynaptic and heterosynaptic structural plasticity of dendritic spines in abGCs following 2-h stimulation of the perforant path *in vivo*. This provides structural evidence for synaptic plasticity in abGCs, consistent with abGCs having an active role in hippocampal learning and memory (2). In addition, we describe heterosynaptic structural plasticity of spines in mGCs.

Two-hour HFS of the MPP led to LTP, associated with a strong Arc expression in the GCL. The stimulated MML exhibited an

increase in F-actin expression as well as a significant enlargement of dendritic spines in abGCs from 28 dpi on, thus revealing robust and layer-specific molecular and structural correlates of homosynaptic LTP in young abGCs. In addition, homosynaptic LTP following 2-h HFS of the MPP was accompanied by heterosynaptic LTD, as shown by control stimulation of the LPP. Furthermore, the expression of F-actin was reduced in the adjacent unstimulated OML, the termination site of the LPP, as well as in the unstimulated IML. Dendritic spines of abGCs in the IML and OML showed a significant reduction in size from 35 dpi on, indicating heterosynaptic structural plasticity. In addition, homo- and heterosynaptic structural plasticity was also found on the level of individual abGCs from 35 dpi on as well as in mature abGCs at 77 dpi and at similar intensities in developmentally born mGCs.

We conclude that synaptic integration of abGCs into the entorhino-hippocampal pathway is a gradual process requiring at least 4–5 wk until abGCs exhibit structural plasticity comparable to that of mGCs in response to synaptic activation. The finding of layer-specific homo- and heterosynaptic plasticity within the same dendritic tree of individual GCs can be explained as a homeostatic mechanism on the cellular level in both abGCs and mGCs.

General Spine Development of AbGCs. We analyzed the number and morphology of dendritic spines in RV-GFP-labeled abGCs at 21, 28, 35, and 77 dpi and compared them with AAV-GFP-labeled mGCs located in the contralateral, unstimulated DG. The number of spines increased from 21 dpi on, reaching a maximum density at 77 dpi with no significant differences from mGCs (Fig. 2). The percentage of large spines was almost constant, between 10–15%, throughout all analyzed age groups, indicating that the rate of de novo formation of spines is proportional to their morphological development. Our data are consistent with earlier reports from rats and mice on the time course of spinogenesis in abGCs. The earliest time point of spine formation in abGCs was reported at 16 dpi for rats (35) and mice (15). An early sharp increase in spine density was observed between

16 and 18 dpi in rats (35) and about 1 wk later in mice (15, 17), supporting the general idea that abGCs mature faster in rats than in mice (36). Reports in mice further showed a continuous increase during the following 8 wk until abGCs reached a plateau at about 70 dpi. Spines can show a prolonged structural maturation, which is modulated by a variety of stimuli (15, 17, 37). Because in our study abGCs at 77 dpi exhibited spine shapes and numbers comparable to mGCs, we conclude that in rats spine maturation is completed by 11 wk.

The characterization of spine formation in maturing abGCs is based on the analysis of dendritic segments located in the contralateral DG. The contralateral DG receives limited input from the ipsilateral entorhinal cortex (EC) via direct commissural and indirect multisynaptic projections. The first pathway is known to evoke only a sparse activation of GCs lacking the capacity for LTP induction under normal, physiological conditions (38–41). Our electrophysiological data showed a strong LTP induction of the ipsilateral EC–DG pathway and no LTP induction on the contralateral EC–DG pathway (Fig. 1C). Furthermore, the contralateral, nonstimulated DG showed no enhancement of Arc expression in the GCL (Fig. 1) as well as no enhancement of F-actin compared with control animals (Fig. 3) in all stimulation experiments. This clearly indicates the absence of any direct or indirect (multisynaptic) stimulation strong enough to induce LTP resulting in relevant changes in spine size. However, any possible indirect stimulation of the contralateral DG would likely lead to a potential overestimation of contralateral spine sizes and thus would lead to an underestimation of the documented effects on the ipsilateral side. We therefore chose the contralateral DG as a valuable control that allowed a direct comparison of the nonstimulated and stimulated side in each animal.

Induction of Homo- and Heterosynaptic Plasticity Following 2-h HFS of the MPP. Two types of synaptic plasticity are the focus of this paper: homosynaptic plasticity (potentiation), which is input specific and occurs only at directly activated synapses, and heterosynaptic plasticity (depression), which can be induced at synapses that were not activated during the induction of homosynaptic plasticity (26). Both forms of plasticity have been well studied in the DG and can be induced by stimulation of the perforant path *in vivo* (28, 30, 42). Heterosynaptic plasticity has been discussed as a homeostatic mechanism for normalization of synaptic weights and maintenance of synaptic competition (27).

In our experiments, HFS of the MPP induced a robust homosynaptic LTP and heterosynaptic LTD of the LPP, as reported earlier by Abraham et al. (26, 43). LTP induction was accompanied by a layer-specific accumulation of F-actin in the stimulated MML, which is in agreement with the observations described by Fukazawa et al. (29) indicating that the applied stimulation protocol and procedure were specific in targeting fibers of the MPP and mainly activated synapses located in the MML. Furthermore, all effects could be blocked by the NMDA receptor antagonist MK-801 (see below). Our findings are well in line with Fukazawa et al. (29), who showed that LTP induction in the DG by stimulating the perforant path *in vivo* leads to a long-lasting NMDA receptor-dependent reorganization of F-actin. Intriguingly, we also found a significant decrease in F-actin in the adjacent unstimulated IML and OML after stimulation of the MML. F-actin, as a component of the cytoskeleton, is associated with the plasma membrane and organization of the PSD in dendritic spines and plays a crucial role in synaptic plasticity and the definition of spine morphology (44). Polymerization of actin filaments is required for stable LTP (21, 45), whereas LTD is accompanied by depolymerization of F-actin (46). Thus, our data suggest that actin could be involved in the regulation not only of homosynaptic LTP but also of heterosynaptic LTD.

Given the well-described role of F-actin in synaptic plasticity, we conclude that the HFS protocol used in our study was suitable to

induce a robust input-specific homosynaptic structural LTP at directly stimulated GC synapses of the MML (29) and likely a concurrent heterosynaptic structural LTD at the unstimulated GC synapses in the OML (26) and possibly also in the IML (42, 47).

Homo- and Heterosynaptic Structural Changes in Spines in AbGCs Following 2-h HFS. We observed an enlargement of spines in dendritic segments located in the stimulated MML in abGCs from 28 dpi on and shrinkage of spines in the adjacent nonstimulated IML and OML from 35 dpi on. Spine size is directly correlated with the size of the PSD and the number of glutamate receptors and thus with synaptic strength (18–20). Induction of LTP is associated with spine enlargement (21), and LTD is associated with spine shrinkage (22). Induction of homosynaptic LTP and heterosynaptic LTD at the perforant path synapse should consequently manifest as a change in spine size, as found in our study. It is heavily debated if LTP is accompanied by a *de novo* formation of spines or morphological changes in preexisting spines (48, 49). In fact, this may depend on the plasticity-inducing protocols used in different studies. We could not see a change in the overall number of spines following stimulation, indicating that our LTP protocol did not induce changes in spine density. Importantly, tracing dendritic segments from the cell soma to the hippocampal fissure allowed us to study structural changes following HFS in the IML, MML, and OML within the same cell. GCs with induced heterosynaptic plasticity were identified by showing an enlargement of spines in the MML and shrinkage of spines in the IML and OML in comparison with the contralateral, nonstimulated hemisphere. Heterosynaptic plasticity has been reported previously only in the MML and OML, but not in the IML, of the DG. Therefore, these results provide not only evidence for heterosynaptic plasticity in abGCs but also experimental evidence for heterosynaptic plasticity at commissural/associational IML synapses, as has been predicted by computational modeling (47). We found stimulation-induced layer-specific homo- and heterosynaptic plasticity on neighboring IML, MML, and OML segments of the dendritic tree in individual abGCs and mGCs. The effective relative change in structural spine plasticity was equal among all groups. Interestingly, the percentage of large spines in abGCs and mGCs showed no net change along the dendritic tree compared with unstimulated control GCs. Thus, heterosynaptic shrinkage of spines counteracted homosynaptic spine enlargement. These findings support the idea of heterosynaptic plasticity as a homeostatic mechanism for normalization of synaptic weights (27).

NMDA Receptor-Dependent Heterosynaptic Plasticity. Our results demonstrate a comprehensive effect of the NMDA receptor antagonist MK-801 in blocking both homo- and heterosynaptic plasticity at the level of electrophysiology, expression of plasticity-related genes, reorganization of actin, and structural changes of dendritic spines. It has been demonstrated previously that NMDA receptors are critically involved in the induction of heterosynaptic plasticity and the structural remodeling of dendritic spines. Abraham et al. (34) demonstrated that application of MK-801 successfully blocked the induction of LTP at the MPP in anesthetized rats. In a follow-up study the NMDA receptor antagonist 3-(2-Carboxypiperazin-4-yl)propyl-1-phosphonic acid (CPP) was used to block the induction of homosynaptic LTP and heterosynaptic LTD (50) at the perforant path. Additionally, Fukazawa et al. (29) blocked the accumulation of F-actin in the stimulated MML of the DG following stimulation. Our study thus confirms and extends these previous findings. In addition, as stimulation-induced effects were blocked by MK-801 on all levels of our analysis, this provides further evidence that the structural homo- and heterosynaptic plasticity found in our study is indeed NMDA receptor dependent and thus represents the structural equivalent of LTP and LTD.

The Time Course of Synaptic Plasticity and Integration of abGCs. In this study homo- and heterosynaptic structural remodeling of spines was analyzed in dendritic segments of labeled GCs. This enabled us to quantify spine changes in individual cells. About 60% of abGCs exhibited homosynaptic increase and heterosynaptic shrinkage of spines from 35 dpi on (Fig. 7), with no further change from 35 to 77 dpi or in comparison with developmentally born GCs. The majority of abGCs showed a transition from homosynaptic plasticity without heterosynaptic plasticity at 28 dpi to homosynaptic plasticity together with concurrent heterosynaptic plasticity from 35 dpi on. In a previous study, we analyzed the time course of LTP induction by the expression of IEGs in abGCs following 2-h HFS of the perforant path in adult rats (32). De novo transcription of IEGs (e.g., *c-fos* and *Arc*) has been shown to be required for long-lasting LTP and synaptic plasticity (51, 52). We identified a sharp increase in the ability of abGCs to respond to LTP stimulation with the expression of IEGs between 28 and 35 dpi (32). In line with our data, evidence of early local connections to the hippocampal network has been reported, as well as long-range afferent projections from the EC via the perforant path in a rapidly increasing quantity from 21 dpi on, by using rabies virus-mediated retrograde tracing (6, 53). Taken together, our findings imply a gradual appearance of synaptic plasticity from 21 dpi on and a sharp increase in synaptic integration of abGCs between 28 and 35 dpi.

Between 3 and 6 wk of cell age, abGCs pass through a critical time window that is characterized by a transiently enhanced synaptic plasticity with a lowered threshold for LTP that was NR2B-containing NMDA receptor-dependent (10, 11). This is based on both active and passive membrane properties (8, 54) and on developmentally regulated synaptic expression of NR2B-containing NMDA receptors at 4 wk but not 8 wk of cell age (9). In addition, during the critical phase, coupling and response-to-feedback inhibition through GABAergic interneurons is weak, but during maturation GCs become gradually integrated into inhibitory circuits (13). In line with these functional studies, we provide detailed *in vivo* evidence on the cellular level for the ability of new GCs to react with structural homosynaptic plasticity to LTP from 28 dpi on. We extend previous data by showing structural heterosynaptic plasticity to concurrent LTD induction from 35 dpi on. Although we found a clear increase in spine plasticity at 4–5 wk of cell age, consistent with a functional integration during this phase, we did not detect any signs of transiently enhanced plasticity compared with older abGCs or mGCs that would support the concept of a critical phase of enhanced plasticity. However, the homo- and heterosynaptic structural plasticity of spines found in this study might not entirely reflect functional changes in synaptic strength. Thus, further functional studies, preferably combined with computational modeling (54), are needed to determine whether synapses weaken or strengthen proportionally to spine size in an equal manner in young and mature abGCs and mGCs.

Based on our structural data, we favor the concept of a sudden appearance (clear onset) followed by a gradual increase in the proportion abGCs displaying synaptic plasticity and integration with increasing cell age. This concept is founded on the following observations on abGCs in rats *in vivo*: By 21 dpi, abGCs show matured dendritic trees and total dendritic lengths comparable to those of mature abGCs and mGCs, indicating that structural dendritic maturation precedes functional integration (55). The number of spines gradually increases in all parts of the ML from 21 dpi to 77 dpi, when abGCs reach mGC levels of spine density. Homosynaptic structural plasticity develops by 28 dpi, followed by heterosynaptic plasticity at 35 dpi, and no further increase at 77 dpi. These data are in line with our previous observation of a cell age-dependent gradual increase in IEG reactivity to HFS and LTP induction in abGCs (32).

We conclude that during their development abGCs pass through a process of structural maturation until the third week,

followed by a gradual integration into the hippocampal network between 4–5 wk of age and further synaptic maturation until 11 wk when abGCs appear to be comparable to developmentally born mGCs. The finding of robust homo- and heterosynaptic structural plasticity during the time period of synaptic integration is consistent with the general view that abGCs contribute to hippocampus-specific forms of learning and memory (2).

Methods

Full descriptions of the experimental procedures are presented in *SI Methods*.

Animals. Adult male Sprague–Dawley rats (8–13 wk old, 220–450 g; Charles River) were housed under standard laboratory conditions. All animal experiments were performed in conformance with German guidelines for the use of laboratory animals and were approved by the institutional review board responsible for our institution (Regierungspräsidium Darmstadt), as well as by the animal welfare officer of our institution (Institute of Clinical Neuroanatomy, Goethe University Frankfurt).

Retrovirus Production. HEK293T cells were cotransfected with pCAG-GFP, pCMV-GP, and pCMV-VSV-G (3:2:1) plasmids by calcium phosphate precipitation. The medium containing retrovirus was collected 48 h after transfection. Cell debris was removed from the supernatant by centrifugation at $3,200 \times g$ for 10 min and filtration through a 0.22- μm filter. The retrovirus was concentrated by ultracentrifugation at $160,000 \times g$ for 2 h (Sorvall WX Ultracentrifuge and SureSpin 630 swinging bucket rotor; Thermo Fisher Scientific). The retroviral pellet was resuspended in 200 μL of PBS (Sigma-Aldrich), aliquoted, and stored at -80°C . The titer was at 10^5 cfu.

AAV Production. HEK293T cells were cotransfected with pDP1rs, pDG, and GFP-vector plasmid (6:4:1) by calcium phosphate precipitation. The transfected cells were collected 48 h after transfection. Cells were washed two times by centrifugation at $1,500 \times g$ for 5 min and were resuspended in PBS. The viral particles inside the cells were set free by multiple freeze-thaw cycles (four times). The supernatant was collected and washed by centrifugation at $3,200 \times g$ for 10 min. The AAV-containing supernatant was aliquoted and stored at -80°C .

Intrahippocampal Viral *In Vivo* Injection. All surgical procedures were performed under deep anesthesia [150 μg medetomidin (Domitor; Pfizer), 2 mg midazolam (Dormicum; Roche), and 5 μg fentanyl (Janssen Pharmaceutica) per kilogram body weight *i.m.* initially with additional injections as needed], in agreement with the German law on the use of laboratory animals. Animals were placed in a Kopf stereotaxic device (Kopf Instruments). Two small holes (1.5–2.0 mm diameter) were drilled in the skull at -3.8 mm from bregma and 2.2 mm laterally in both hemispheres. A NanoFil syringe (World Precision Instruments, Inc.) with a 35-gauge beveled needle (NF35BV-2; World Precision Instruments) was used to slowly inject 0.75 μL of the viral solution into the DG of both hemispheres at 3.2 mm and 3.7 mm below the brain surface.

Perforant Path Stimulation *In Vivo*. All surgical procedures for perforant path stimulation were performed under deep urethane anesthesia [250 mg urethane/mL 0.9% saline (Sigma-Aldrich), 1.25 g/kg body weight *s.c.* initially with additional injections as needed], in agreement with the German law on the use of laboratory animals. Surgery and HFS procedures were performed as previously described (32).

In an additional experimental group of AAV-GFP-transduced animals ($n = 6$), the uncompetitive NMDA receptor antagonist Dizocilpine maleate (MK-801; Sigma-Aldrich) was injected *i.p.* (2 mg/kg body weight) 150 min before HFS and repeatedly (0.5 mg/kg body weight) at 30-min intervals starting 30 min before HFS to maintain the working concentration. Evoked field potentials of the MPP and LPP were recorded bilaterally before, during, and following 2-h HFS as described above. Rats were transcardially perfused with 4% paraformaldehyde (PFA).

Control animals ($n = 8$) were deeply anesthetized with urethane and were transcardially perfused with 4% PFA. Brains were removed, postfixed for up to 18 h, and prepared for histological examination of F-actin (Fig. 3C).

Immunohistochemistry. Free-floating sections were washed in TBS, blocked with 5% BSA (New England BioLabs) containing 0.1% Triton X-100 for 1 h at room temperature to reduce nonspecific staining, and incubated in primary antibody solution containing 2% BSA, 0.25% Triton X-100, and 0.1% NaN_3 in 0.1 M Tris-buffered saline (TBS) for 48 h at room temperature. The following primary antibodies were used: rabbit polyclonal anti-Arc (1:1,000; Synaptic

Systems) and mouse anti-GFP488 (1:500; fluorescence-labeled Alexa 488; Sigma-Aldrich). For immunohistochemical detection of fluorescence, sections were incubated with secondary fluorescence-labeled antibodies (Alexa 488 and Alexa 568, 1:1,000; Vector Labs) for 24 h at room temperature.

For detection of F-actin, free-floating sections were washed in TBS, blocked with 5% BSA for 1 h at room temperature, and incubated with Phalloidin-Alexa 568 (1:200; MoBiTec) for 24 h at room temperature.

Statistical Analysis. Data management, statistical analysis, and visualization were done with Microsoft Excel (Microsoft) and GraphPad Prism 6 (GraphPad Software). Statistical comparisons were calculated with the two-sided Wilcoxon rank-sum test (Figs. 3–7 and Fig. S1), Kruskal–Wallis with Dunn’s comparison test (Figs. 2 and 6), two-way ANOVA with Bonferroni correction (Figs. 3 and 6),

or the Friedman with Dunn’s multiple comparison test (Fig. 2). The significance level was set at $P < 0.05$. Group values are reported as means \pm SEM.

ACKNOWLEDGMENTS. We thank Ute Fertig and Anke Biczysko for technical assistance in preparing and staining hippocampal slices and electron microscopy. This work was supported by Deutsche Forschungsgemeinschaft Grant CRC 1080 and JE 528/6-1, Alzheimer Forschung Initiative 15038, Dr. Senckenbergische Stiftung, August Scheidel-Stiftung, and Marie Christine Held and Erika Hecker-Stiftung Grants, the Landes-Offensive zur Entwicklung Wissenschaftlich-ökonomischer Exzellenz Program of the Center for Personalized Translational Epilepsy Research, the International Max-Planck Research School for Neural Circuits in Frankfurt, and German Federal Ministry of Education and Research Grant 01GQ1406 (Bernstein Award 2013). Parts of this work were the subject of the doctoral theses of M.B. and T.J.

- Gage FH (2000) Mammalian neural stem cells. *Science* 287:1433–1438.
- Cameron HA, Glover LR (2015) Adult neurogenesis: Beyond learning and memory. *Annu Rev Psychol* 66:53–81.
- Clelland CD, et al. (2009) A functional role for adult hippocampal neurogenesis in spatial pattern separation. *Science* 325:210–213.
- Nakashiba T, et al. (2012) Young dentate granule cells mediate pattern separation, whereas old granule cells facilitate pattern completion. *Cell* 149:188–201.
- Kempermann G, Song H, Gage FH (2015) Neurogenesis in the adult hippocampus. *Cold Spring Harb Perspect Biol* 7:a018812.
- Deshpande A, et al. (2013) Retrograde monosynaptic tracing reveals the temporal evolution of inputs onto new neurons in the adult dentate gyrus and olfactory bulb. *Proc Natl Acad Sci USA* 110:E1152–E1161.
- Denny CA, et al. (2014) Hippocampal memory traces are differentially modulated by experience, time, and adult neurogenesis. *Neuron* 83:189–201.
- Schmidt-Hieber C, Jonas P, Bischofberger J (2004) Enhanced synaptic plasticity in newly generated granule cells of the adult hippocampus. *Nature* 429:184–187.
- Ge S, Yang C-H, Hsu K-S, Ming G-L, Song H (2007) A critical period for enhanced synaptic plasticity in newly generated neurons of the adult brain. *Neuron* 54:559–566.
- Wang S, Scott BW, Wojtowicz JM (2000) Heterogenous properties of dentate granule neurons in the adult rat. *J Neurobiol* 42:248–257.
- Snyder JS, Kee N, Wojtowicz JM (2001) Effects of adult neurogenesis on synaptic plasticity in the rat dentate gyrus. *J Neurophysiol* 85:2423–2431.
- Marin-Burgin A, Mongiat LA, Pardi MB, Schinder AF (2012) Unique processing during a period of high excitation/inhibition balance in adult-born neurons. *Science* 335:1238–1242.
- Temprana SG, et al. (2015) Delayed coupling to feedback inhibition during a critical period for the integration of adult-born granule cells. *Neuron* 85:116–130.
- Bergami M, et al. (2015) A critical period for experience-dependent remodeling of adult-born neuron connectivity. *Neuron* 85:710–717.
- Zhao C, Teng EM, Summers RG, Jr, Ming G-L, Gage FH (2006) Distinct morphological stages of dentate granule neuron maturation in the adult mouse hippocampus. *J Neurosci* 26:3–11.
- Toni N, Sultan S (2011) Synapse formation on adult-born hippocampal neurons. *Eur J Neurosci* 33:1062–1068.
- Toni N, et al. (2007) Synapse formation on neurons born in the adult hippocampus. *Nat Neurosci* 10:727–734.
- Nusser Z, et al. (1998) Cell type and pathway dependence of synaptic AMPA receptor number and variability in the hippocampus. *Neuron* 21:545–559.
- Harris KM, Jensen FE, Tsao B (1992) Three-dimensional structure of dendritic spines and synapses in rat hippocampus (CA1) at postnatal day 15 and adult ages: Implications for the maturation of synaptic physiology and long-term potentiation. *J Neurosci* 12:2685–2705.
- Kasai H, Matsuzaki M, Noguchi J, Yasumatsu N, Nakahara H (2003) Structure-stability-function relationships of dendritic spines. *Trends Neurosci* 26:360–368.
- Matsuzaki M, Honkura N, Ellis-Davies GCR, Kasai H (2004) Structural basis of long-term potentiation in single dendritic spines. *Nature* 429:761–766.
- Zhou Q, Homma KJ, Poo MM (2004) Shrinkage of dendritic spines associated with long-term depression of hippocampal synapses. *Neuron* 44:749–757.
- Oh WC, Parajuli LK, Zito K (2015) Heterosynaptic structural plasticity on local dendritic segments of hippocampal CA1 neurons. *Cell Rep* 10:162–169.
- Amaral DG, Scharfman HE, Lavenex P (2007) The dentate gyrus: Fundamental neuroanatomical organization (dentate gyrus for dummies). *Prog Brain Res* 163:3–22.
- Steward O, Wallace CS, Lyford GL, Worley PF (1998) Synaptic activation causes the mRNA for the IEG Arc to localize selectively near activated postsynaptic sites on dendrites. *Neuron* 21:741–751.
- Abraham WC, Logan B, Wolff A, Benuskova L (2007) “Heterosynaptic” LTD in the dentate gyrus of anesthetized rat requires homosynaptic activity. *J Neurophysiol* 98:1048–1051.
- Chistiakova M, Bannon NM, Chen J-Y, Bazhenov M, Volgushev M (2015) Homeostatic role of heterosynaptic plasticity: Models and experiments. *Front Comput Neurosci* 9:89.
- Jedlicka P, Benuskova L, Abraham WC (2015) A voltage-based STDP rule combined with fast BCM-like metaplasticity accounts for LTP and concurrent “heterosynaptic” LTD in the dentate gyrus in vivo. *PLoS Comput Biol* 11:e1004588.
- Fukazawa Y, et al. (2003) Hippocampal LTP is accompanied by enhanced F-actin content within the dendritic spine that is essential for late LTP maintenance in vivo. *Neuron* 38:447–460.
- Abraham WC, Bliss TVP, Goddard GV (1985) Heterosynaptic changes accompany long-term but not short-term potentiation of the perforant path in the anaesthetized rat. *J Physiol* 363:335–349.
- Petersen RP, et al. (2013) Electrophysiological identification of medial and lateral perforant path inputs to the dentate gyrus. *Neuroscience* 252:154–168.
- Jungenitz T, Radic T, Jedlicka P, Schwarzacher SW (2014) High-frequency stimulation induces gradual immediate early gene expression in maturing adult-generated hippocampal granule cells. *Cereb Cortex* 24:1845–1857.
- Deller T, et al. (2003) Synaptotagmin-deficient mice lack a spine apparatus and show deficits in synaptic plasticity. *Proc Natl Acad Sci USA* 100:10494–10499.
- Abraham WC, Mason SE (1988) Effects of the NMDA receptor/channel antagonists CPP and MK801 on hippocampal field potentials and long-term potentiation in anesthetized rats. *Brain Res* 462:40–46.
- Ohkawa N, et al. (2012) Spine formation pattern of adult-born neurons is differentially modulated by the induction timing and location of hippocampal plasticity. *PLoS One* 7:e45270.
- Snyder JS, et al. (2009) Adult-born hippocampal neurons are more numerous, faster maturing, and more involved in behavior in rats than in mice. *J Neurosci* 29:14484–14495.
- Toni N, et al. (2008) Neurons born in the adult dentate gyrus form functional synapses with target cells. *Nat Neurosci* 11:901–907.
- Wilson RC, Levy WB, Steward O (1979) Functional effects of lesion-induced plasticity: Long term potentiation in formal and lesion-induced temporodentate connections. *Brain Res* 176:65–78.
- Wilson RC, Levy WB, Steward O (1981) Changes in translation of synaptic excitation to dentate granule cell discharge accompanying long-term potentiation. II. An evaluation of mechanisms utilizing dentate gyrus dually innervated by surviving ipsilateral and sprouted crossed temporodentate inputs. *J Neurophysiol* 46:339–355.
- Wilson RC (1981) Changes in translation of synaptic excitation to dentate granule cell discharge accompanying long-term potentiation. I. Differences between normal and reinnervated dentate gyrus. *J Neurophysiol* 46:324–338.
- Alvarez-Salvado E, Pallarés V, Moreno A, Canals S (2013) Functional MRI of long-term potentiation: Imaging network plasticity. *Philos Trans R Soc Lond B Biol Sci* 369:20130152.
- Benuskova L, Abraham WC (2007) STDP rule endowed with the BCM sliding threshold accounts for hippocampal heterosynaptic plasticity. *J Comput Neurosci* 22:129–133.
- Abraham WC, Goddard GV (1983) Asymmetric relationships between homosynaptic long-term potentiation and heterosynaptic long-term depression. *Nature* 305:717–719.
- Bosch M, Hayashi Y (2012) Structural plasticity of dendritic spines. *Curr Opin Neurobiol* 22:383–388.
- Kim CH, Lisman JE (1999) A role of actin filament in synaptic transmission and long-term potentiation. *J Neurosci* 19:4314–4324.
- Okamoto K, Nagai T, Miyawaki A, Hayashi Y (2004) Rapid and persistent modulation of actin dynamics regulates postsynaptic reorganization underlying bidirectional plasticity. *Nat Neurosci* 7:1104–1112.
- Benuskova L, Jedlicka P (2012) Computational modeling of long-term depression of synaptic weights: Insights from stdp, metaplasticity and spontaneous activity. *Neural Netw World* 22:161–180.
- Popov VI, et al. (2004) Remodelling of synaptic morphology but unchanged synaptic density during late phase long-term potentiation (LTP): A serial section electron micrograph study in the dentate gyrus in the anaesthetized rat. *Neuroscience* 128:251–262.
- Wosiski-Kuhn M, Stranahan AM (2012) Transient increases in dendritic spine density contribute to dentate gyrus long-term potentiation. *Synapse* 66:661–664.
- Christie BR, Abraham WC (1992) NMDA-dependent heterosynaptic long-term depression in the dentate gyms of anaesthetized rats. *Synapse* 10:1–6.
- Bramham CR, Worley PF, Moore MJ, Guzowski JF (2008) The immediate early gene *arc/arg3.1*: Regulation, mechanisms, and function. *J Neurosci* 28:11760–11767.
- Fleischmann A, et al. (2003) Impaired long-term memory and NR2A-type NMDA receptor-dependent synaptic plasticity in mice lacking c-Fos in the CNS. *J Neurosci* 23:9116–9122.
- Vivar C, et al. (2012) Monosynaptic inputs to new neurons in the dentate gyrus. *Nat Commun* 3:1107.
- Beining M, Mongiat LA, Schwarzacher SW, Cuntz H, Jedlicka P (2017) T2N as a new tool for robust electrophysiological modeling demonstrated for mature and adult-born dentate granule cells. *eLife* 6:e26517.
- Beining M, et al. (2017) Adult-born dentate granule cells show a critical period of dendritic reorganization and are distinct from developmentally born cells. *Brain Struct Funct* 222:1427–1446.
- Schindelin J, et al. (2012) Fiji: An open-source platform for biological-image analysis. *Nat Methods* 9:676–682.